NJC

Accepted Manuscript

ROYAL SOCIETY OF CHEMISTRY

www.rsc.org/njc

Graphical Abstract:
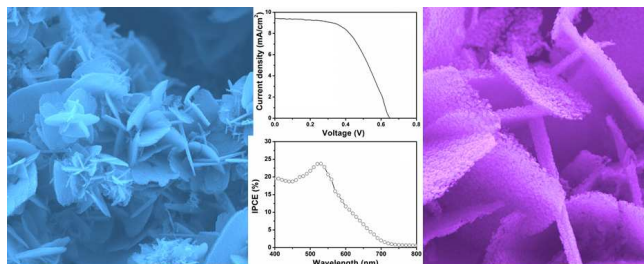
Facile and direct growth of highly porous ZnO nanosheets self-assembled in rosette like morphologies on ITO for high-performance dye-sensitized solar cell application.

Highly porous ZnO nanosheets self-assembled in rosette like morphologies for dye sensitized solar cell application

Ahmad Umar,[1,2]* Mohammad Shaheer Akhtar,[3] Mohammed Sultan Al-Assiri,[2,4] Ali Al-Hajry, [2,4] Hamed Algarni,[5] Vagner Romito de Mendonça,[6] Yoshitake Masuda,[7] Sang Hoon Kim,[1,2] Qazi Inamur Rahman[8]

[1] *Department of Chemistry, Faculty of Sciences and Arts, Najran University, Najran University, P.O. Box 1988, Najran, 11001, Kingdom of Saudi Arabia*

[2] *Promising Centre for Sensors and Electronic Devices (PCSED), Najran University, P.O. Box 1988, Najran, 11001, Kingdom of Saudi Arabia*

[3]*New and Renewable Energy Materials Development Center (New REC), Chonbuk National University, South Korea*

[4]*Department of Physics, Faculty of Sciences and Arts, Najran University, Najran University, P.O. Box 1988, Najran, 11001, Kingdom of Saudi Arabia*

[5] *Department of Physics, Faculty of Science, King Khalid University, P. O. Box 9004, Abha, Kingdom of Saudi Arabia*

[6]*Federal Institute of Education, Science and Technology of São Paulo, 18208-000, Itapetininga-SP, Brazil.*

[7]*National Institute of Advanced Industrial Science and Technology (AIST), 2266-98 Anagahora, Shimoshidami, Moriyama-ku, Nagoya 463-8560, Japan*

[8]*Department of Applied Science, Jahangirabad Institute of Technology, Barabanki-225203, India*

*Authors to whom correspondence should be addressed;

E-mail: ahmadumar786@gmail.com (A. Umar)

Tel: +966-534-574-597

Fax: +966-7-5442-135

Abstract

This paper reports a facile low-temperature hydrothermal process to grow highly porous ZnO nanosheets, self-assembled in rosette like morphology, over the transparent indium tin oxide (ITO) glass substrate for dye-sensitized solar cell application. The prepared porous nanosheets were examined in detail using several techniques to understand the morphological, structural, compositional, optical and photovoltaic properties. The detailed morphological investigations revealed that the prepared nanosheets were made by the accumulation of small ZnO nanoparticles with the typical diameters of 28 ± 3 nm. A systematic growth process to prepare such ZnO nanosheets is also discussed in terms of chemical reactions involved. The prepared nanosheets possess the stoichiometric elemental ratios of Zn and oxygen and exhibiting good crystallinity and wurtzite hexagonal phase along with good optical properties. Further, the prepared ZnO nanosheets on ITO substrates were directly utilized as photo-anode to fabricate efficient dye sensitized solar cell (DSSC) which demonstrated a reasonable light-to-electricity conversion efficiency of ~3.4% with high short circuit current (J_{SC}) of 9.45 mA/cm^2, open circuit voltage (V_{OC}) of 0.654 and fill factor of 0.55. The obtained J_{SC} and the performance of fabricated DSSC are attributed to the high surface to volume ratio of porous ZnO nanosheets, which deliver the high light harvesting efficiency.

Key words: ZnO, nanosheets, rosette, porous, dye-sensitized solar cells, optical properties

1. Introduction

A relatively low cost photo-electrochemical solar cell device, called dye-sensitized solar cell (DSSC) is presumed to be the promising alternative to the conventional silicon- based solar cell.[1,2] After the first report in 1991, extensive efforts have been made to enhance the solar-to-electricity conversion efficiencies of DSSCs.[1,2] With over 12% conversion efficiencies of TiO_2-based DSSCs were fabricated by Gratzel's group, close to the conventional solar cells, and reported in the literature.[3] Typically, the DSSCs are composed of three major components, i.e. photoanode, charge transporting redox electrolyte and metal coated counter electrode. The choice of photoanode material is one of the most important factors to fabricate high efficient DSSC; thus, generally metal oxides and based semiconductor materials were used as efficient anode materials for DSSCs.[1-8] In DSSC, the dye molecules absorb sunlight and leads to photoexcitation where the photoexcited electrons inject into the metal oxide and quickly collects at the photoanode.[4] There are several metal oxide semiconductor nanomaterials such as TiO_2, SnO_2, ZnO, Nb_2O_5, etc. which have been used as photoanode materials to fabricate DSSCs.[1-10] It has been observed that the sunlight-to-electricity conversion efficiencies of the DSSCs are also depending upon the morphological, structural and optical properties of the photoanode materials. Few reports demonstrated the mechanistic studies of DSSC based on the specific characteristics of the photoanode (TiO_2) materials.[8-10]

Among various photoanode materials, the II-VI n-type semiconductor ZnO nanomaterials could be considered as an important and potential photoanode materials to fabricate DSSC because of its environment benign nature, low-cost, high purity and crystallinity growth and vast diversity in the morphologies.[11] Further, due to several interesting properties such as wide band

gap (3.37 eV at 300 K), high exciton binding energy (60 meV), biocompatibility, piezoelectricity, etc, ZnO is considered as one of most important multifunctional nanomaterials for variety of applications including sensors, actuators, nano-electronics, optoelectronics, nanogenerators, cancer therapy and detection, DSSCs, electro- and photoluminescence devices and so on.[11-17]

Including other applications, ZnO is considered as promising photoanode material to fabricate efficient DSSC as it possess some specific properties comparable to TiO_2, which exhibited highest light-to-electricity conversion efficiency for DSSC.[1,2,18] There are several reports in the literature which demonstrate the successful use of ZnO nanomaterials as photoanode material for the fabrication of DSSCs.[19-27] ZnO nanorods based DSSC was fabricate by Hsu et al. and reported low light-to-electricity conversion efficiency of 0.22%.[19] Suh et al. fabricated the branched ZnO nanowires based DSSC with conversion efficiency of ~0.46%,[20] which were prepared by high-temperature thermal evaporation process. Similarly, Baxter et al. have fabricated branched ZnO nanowires based DSSC with the light-to-electricity conversion efficiency of 0.5%.[26] In another report, Cheng et al. have demonstrated the fabrication and characterization of hydrothermally grown ZnO nanorods based DSSC with conversion efficiency of 0.6%.[23] Law et al. further reported ZnO nanorods/nanowires based DSSC which revealed relatively good efficiency of 1.5%.[27] Hydrothermally grown ZnO nanoparticles based DSSC with conversion efficiency of ~1.55% was reported by Suliman et al.[28] Umar et al. demonstrated ZnO nanorods based photoanode for DSSC and achieved light to electricity conversion efficiency of 1.86%.[29] Flower-shaped ZnO nanostructures were also used as photoanode material to fabricate DSSC and exhibited light to electricity conversion efficiencies of ~1.9%.[22] Even though, several reports are available regarding the use of ZnO nanomaterials as photoanode material for DSSC but still there is huge concerns for the selection of proper morphologies to

fabricate efficient DSSCs with better light-to-electricity conversion efficiencies. In this regard, it is expected that the use of 2D ZnO nanostructures, such nanosheets, may enhance the conversion efficiencies for the fabricated DSSCs.[30]

This paper reports the facile growth and detailed characterizations of highly porous 2D ZnO nanosheet assembled in rosette like morphologies for dye-sensitized solar cell (DSSC) applications. Interestingly, the porous nanosheets were grown directly on transparent conducting glass (TCO) substrate thus; the complexity of DSSC fabrications such as film formation on TCO substrates, adhesion issues, etc can be avoided. Therefore, this work presents a simple and effective way to prepare highly porous ZnO nanosheets assembled in rosette like morphologies for DSSC application.

2. Experimental details

2.1. Direct growth of highly porous ZnO nanosheets thin film on ITO substrate

Highly porous ZnO nanosheets assembled in rosette like morphologies thin film was grown by hydrothermal process directly on TCO substrate. In a typical reaction process, the precursor solution was prepared by mixing the aqueous solution of 0.05M zinc nitrate hexahydrate (0.05M, $Zn(NO_3)_2.6H_2O$, Sigma-Aldrich) with 0.05M liquid ammonia, both prepared in 75 mL DI water. Afterwards, 0.11g of polyethylene glycol (Sigma-Aldrich, M.W. = 100000) was added in the precursor solution, in which the PEG amount was fixed to 1/10 correspond to the zinc precursor. The resultant solution (75 mL) was stirred for 30 min and then transferred into a Teflon beaker. Few cleaned indium tin oxide (ITO) substrates (1.5 X 1.5 cm) were placed in the bottom of Teflon beaker which was finally placed in the Teflon-lined stainless steel autoclave, tightly sealed it and heated up to 150 °C for 8 hr. After completing the reaction,

the autoclave was naturally cooled at room-temperature and it was observed that the ITO substrates were covered with tightly attached white colored powders. The substrates were then washed with DI water and ethanol, sequentially and then annealed at 250 °C for 2 hr to remove the carbon impurities. Finally, the prepared substrates were examined in detail in terms of their morphological, structural, compositional, optical and photovoltaic properties.

2.2. Characterizations of highly porous ZnO nanosheets thin film on ITO substrate

The deposited highly porous ZnO nanosheets assembled in rosette-like morphologies were characterized by several techniques. The morphologies were investigated by field emission scanning electron microscopy (FESEM; JEOL-JSM-7600F) and transmission electron microscopy (TEM; JEOL-JEM-2100F) equipped with high-resolution TEM. The crystallinity and structural properties of the prepared porous nanosheets were examined by X-ray diffractometer (XRD; PANalytical X'Pert PRO) measured with Cu-Kα radiation (k = 1.54056 Å) at 45 kV and 40 mA in the range of 2θ=20–65° with scan speed of 5°/min. Further, the elemental composition of the deposited film was characterized by energy dispersive spectroscopy (EDS), attached with FESEM. To examine the scattering properties and purity, the deposited nanosheets were further examined by Raman-scattering spectrophotometer (Raman Station 400; Perkin Elmer) in the range of 200-800 cm^{-1}. The surface species and properties of thin film was analyzed by X-ray Photoelectron Spectroscopy analysis (XPS, AXIS-NOVA, Kratos analytical Ltd., UK).

2.3. Fabrication of dye-sensitized solar cell based on highly porous ZnO nanosheets thin film on ITO substrate

To fabricate the DSSC, the prepared thin film of highly porous ZnO nanosheets assembled in rosette like morphologies on ITO substrates was dipped in an ethanolic solution of 0.3 mM ruthenium (II) 535 bis-TBA (N-719, Solaronix) dye for 12 h at room-temperature under dark condition. After dipping for particular time, the ZnO/ITO substrate was washed by ethanol to remove the un-absorbed dye and dried under nitrogen flow. Further, the dye absorbed ZnO/ITO substrate was placed over the platinum (Pt) coated ITO substrate which was acted as counter electrode and both the electrodes were sealed using hot press by 60 µm thick Surlyn sheet (SX 1170-60, Solaronix). The liquid electrolyte, made of 0.5 M LiI, 0.05 mM I_2, and 0.2 M tert-butyl pyridine in acetonitrile, was introduced into the cell through one of the two small holes drilled in the counter electrode. Later, these holes were sealed with small microscopic glass and Surlyn sheet. The active layer of the resulting cell was approximately 0.25 cm^2 (0.5 cm x 0.5 cm).

The performances of fabricated DSSC were analyzed by measuring the current density (J)–voltage (V) curves using a solar stimulator (I-V measurement system, PV measurement Inc. USA). The light source was 1000-W metal halide lamp and its radiant power was adjusted with respect to Si reference solar cell to about one-sun-light intensity (100 mW/cm^2, AM 1.5G). During the measurement, a black tape mask over the cells except active area part was placed to avoid any interference. The incident photon-to-current conversion efficiency (IPCE) was measured by specially designed absorption spectrum response spectroscopy (PV measurements, Inc., USA). IPCE result of the fabricated DSSC was recorded using a 75 W Xe lamp as a monochromatic beam light source with a low chopping frequency. The calibration of IPCE system was done with a standard silicon photodiode before performing the IPCE measurement.

-7-

3. Results and discussion

3.1. Characterizations and properties of highly porous ZnO nanosheets thin film on ITO substrate

Highly porous ZnO nanosheets thin films were directly grown on ITO substrate which used as photoanode materials to fabricate efficient DSSC. The general morphologies of deposited ZnO material on ITO substrate were characterized by FESEM. Figure 1 exhibits the typical FESEM images which revealed the deposited ZnO materials possess rosette-like morphologies. Interestingly, the rosette-like morphologies are uniformly grown on the substrate with very high density in the form of film (fig 1 (a)). It was fascinating to see that the deposited rosette-like morphologies are made by the accumulation of several nanosheets which are arranged in a special fashion that they made rosette-like structures (fig 1 (b)). The average sizes of the nanosheets are in the range of 2-4 µm while the thicknesses are in the range of 40-50 nm. The prepared nanosheets were further examined with high-resolution FESEM and it was very interesting to see that the nanosheets are made by the accumulation of several thousands of nanoparticles (fig. 1 (c) and (d)). The nanoparticles are stacked each other in such a special and particular manner that made sheet like morphologies (fig. 1 (d)). It was also observed that even though nanoparticles are densely packed with each other but still there are many voids among the nanoparticles which made these nanosheets highly porous. Thus, this special highly porous architecture made the nanosheets assembled in rosette-like morphologies as promising material which can be used to fabricate highly efficient DSSC. The detailed morphological properties of the prepared nanosheets were further examined by TEM and HRTEM.

Figure 1: Typical (a and b) low-magnification and (c and d) high-resolution FESEM images of highly porous ZnO nanosheets assembled in rosette-like morphologies thin film grown on ITO substrate by hydrothermal process

Figure 2 exhibits the typical TEM and HRTEM images of as-deposited highly porous ZnO nanosheets. For the TEM analysis, the deposited porous ZnO nanosheets were detached from the ITO substrate through ultrasonication in isopropyl alcohol (IPA) and a drop of IPA

which contains the nanosheet was placed on the TEM grid and examined. Figure 2 (a) and (b)

demonstrate the typical low-magnification TEM images of a side portion of the prepared porous

nanosheets. The TEM images exhibit full consistency with the observed FESEM results in terms

of morphology and revealed that the nanosheets are highly porous. It is clear from the observed

TEM images that the nanosheets are made by the accumulation of several thousands of small

irregular shaped nanoparticles which are joined each other through their surfaces with the

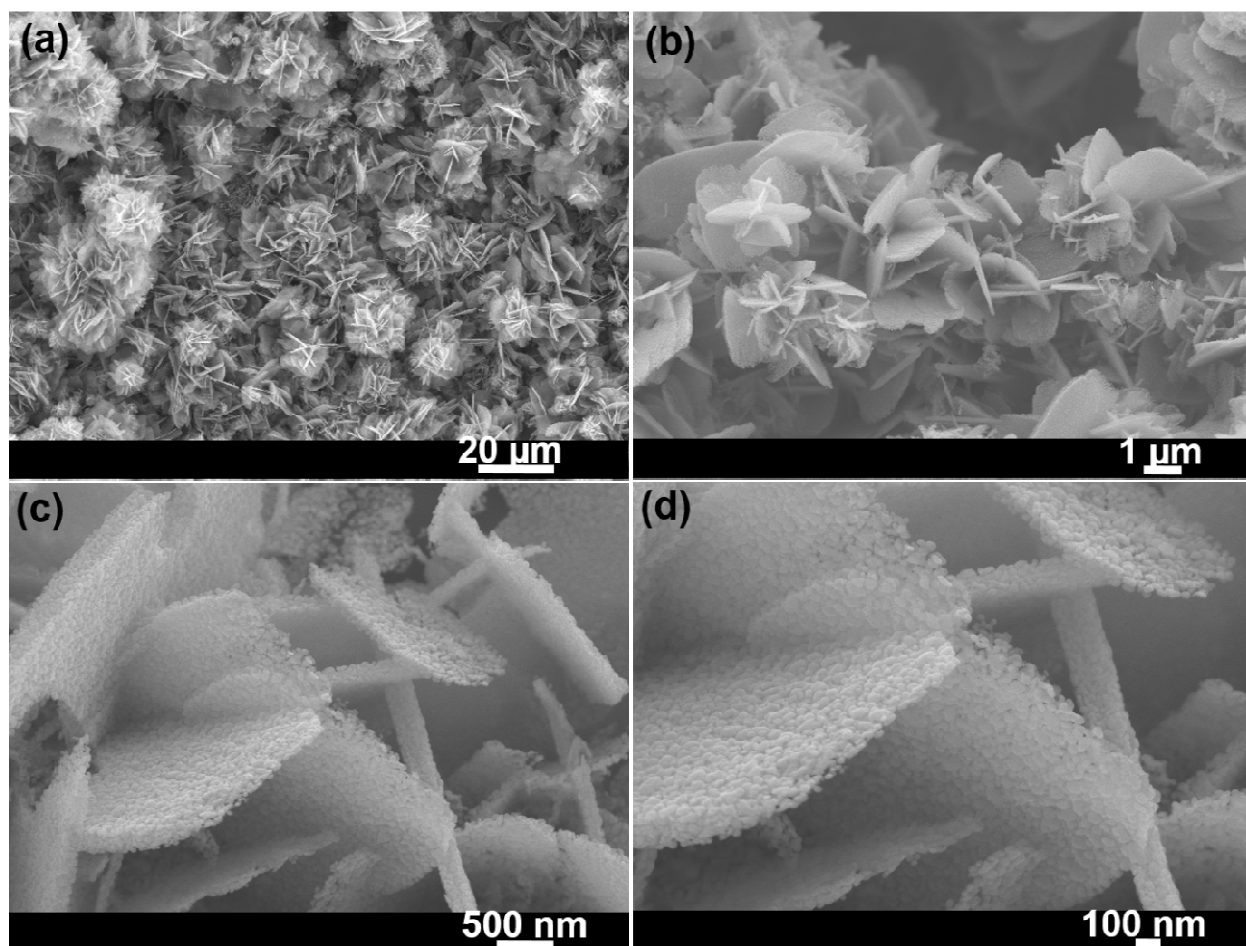adjacent nanoparticles and form the nanosheet like morphologies.
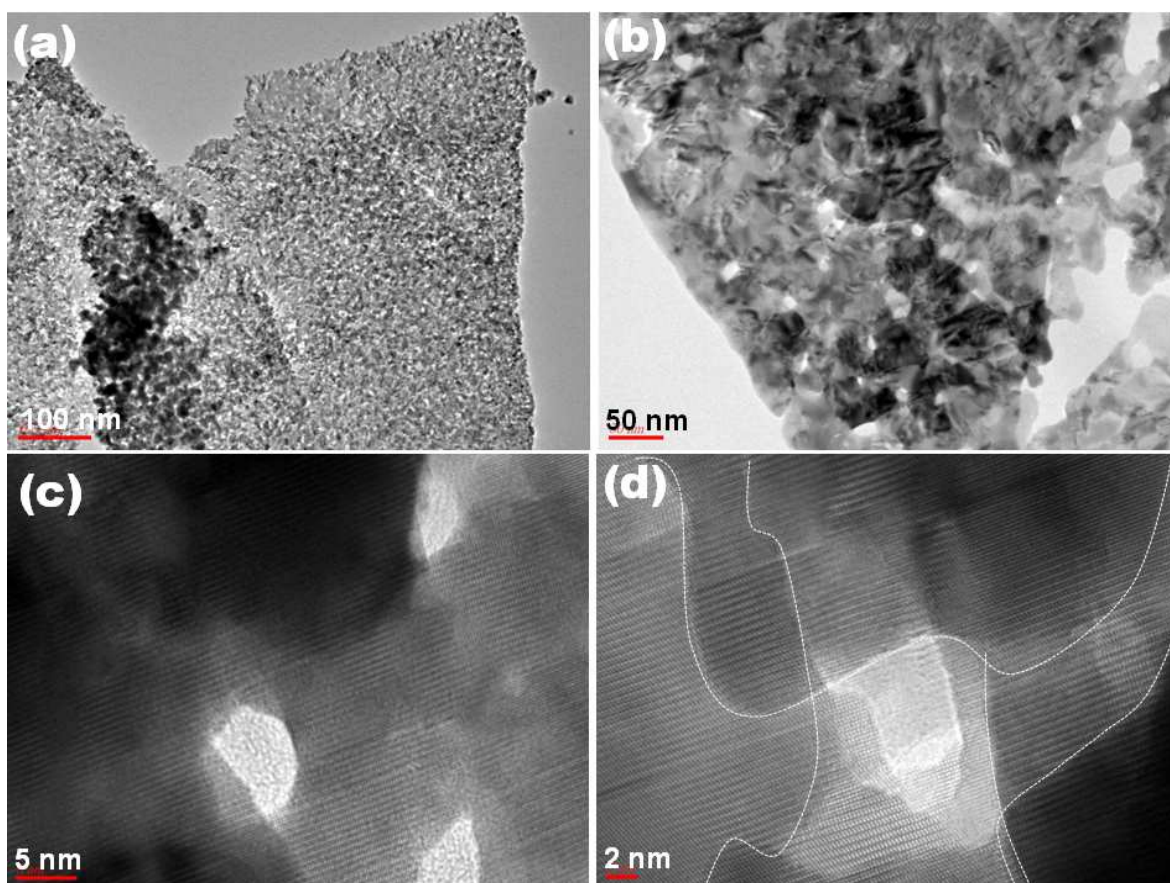

Figure 2: Typical (a and b) low-magnification and (c and d) high-resolution TEM images of
highly porous ZnO nanosheets assembled in rosette-like morphologies thin film grown
on ITO substrate by hydrothermal process

By HRTEM images, it is clear that even though nanoparticles are densely packed with each other but still there are many voids which made these nanosheets highly porous (fig. 2 (c) and (d)). For clear understanding, the nanoparticles outer surfaces are highlighted with white color (fig. 2(d)). Further, the HRTEM images clearly revealed the well-defined lattice fringes with the interplanar distance of 0.52 nm, which is equal to the lattice constant of wurtzite hexagonal ZnO. Thus, it can be confirmed that the prepared nanosheets are well-crystalline and possessing wurtzite hexagonal phase.

Figure 3 depicts the crystallization and deposition process of highly porous ZnO nanosheets assembled in rosette-like morphologies. Basically, the growth process of ZnO nanoparticles can be separated in two steps, i.e. nucleation during the Zn^{2+} hydrolysis followed by a further growth under hydrothermal conditions.[31] As previously described in literature, the hydrolysis of Zn^{2+} under basic conditions yields in small nucleus of a metastable phase of zinc hydroxide.[32] During the hydrothermal growth process, the crystallization and growth of ZnO structures takes place. As reported in the literature, ZnO possess wurtzite anisotropic structures with a preferred growth along the [0001] direction, due to the fact that ZnO (0001) polar surfaces present higher energy comparing with non-polar surfaces.[33] Thus, the growth in a particular direction can be explained by the reduction of total surface energy. However, in the prepared ZnO nanosheets, the crystallographic coherence obtained by Scherrer equation presents isotropic structures, as presented in supplementary S-1.[†] It is noticed that the estimated crystallographic coherences [(100), (002) and (101)] display the average crystallite size around 30 nm of prepared highly porous ZnO nanosheets assembled in rosette-like morphologies. Therefore, it is expected that it may be related to the presence of PEG molecules in the synthesis process during ZnO

crystallization under hydrothermal treatment. As reported, the PEG macromolecules bond with the ZnO solid surface mainly via –OH group of the polar surface of ZnO nanoparticles, which may interact with PEG through hydrogen bonding.[34] Therefore, according to the kinetics of colloid growth, the addition of PEG in the suspension containing ZnO modifies the growth kinetics, leading into isotropic growth in terms of crystallites. PEG adsorption over ZnO surface has been employed to obtain 1D nanostructures,[35] however, the obtainment of such structures is directly related to the PEG concentration.

Over a specific PEG concentration value, spherical nanoparticles are expected to be formed, as occurred in this case. Therefore, it can be proposed that bonding with PEG makes the (0001) surface energy to decrease and prevents the growth in this particular crystallographic direction. It is known that PEG exhibits both hydrophobic and hydrophilic groups. Also, according to the literature,[36] due to the hydrophobic headgroups of PEG (i.e. alcohol groups in PEG), there could be formation of aggregations in the solution. Those formed aggregates acted as templates which lead to the formation nanoparticles. Further, the surfaces of formed nanoparticles possess confined regions and the adjacent nanoparticles undergo a multiplying growth through a cementing mechanism or oriental attachment and finally due to this phenomenon, the sheet-like morphologies were obtained.[31] However, during the formation of nanosheets, the nanoparticles were not assembled in perfect way and their surfaces are not totally matched with the surfaces of the adjacent nanoparticles. Thus, during the multiplying growth and cementing process, the adjacent nanoparticles possess voids which made the nanosheets highly porous and hence finally porous nanosheet morphologies are observed.
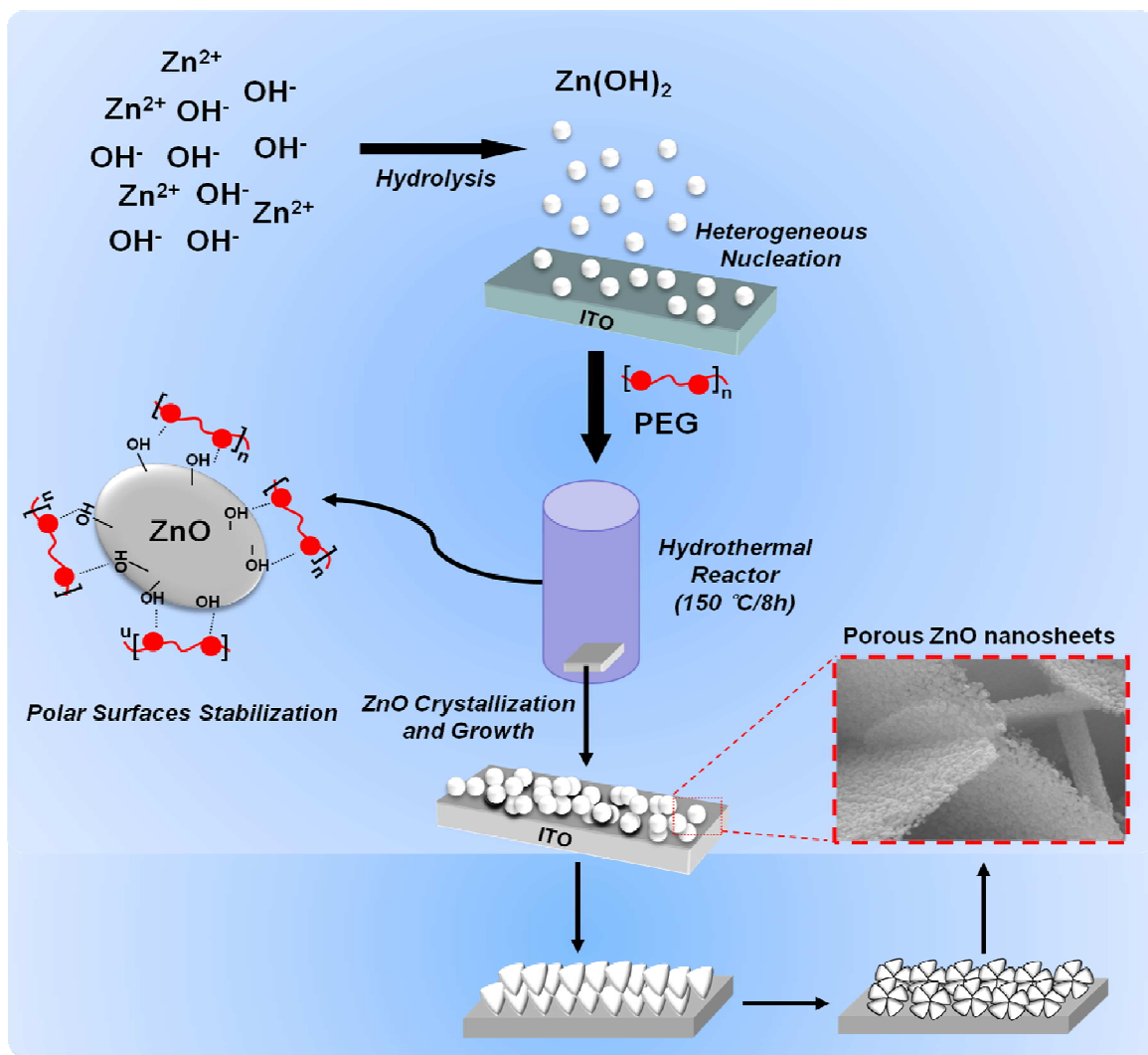
Figure 3: Schematic for the synthesis, crystallization and deposition process of highly porous ZnO nanosheets assembled in rosette-like morphologies.

According to the thermodynamic principle, the polar faces with surface dipoles are thermodynamically less stable compared to non-polar faces which repeatedly go through the rearrangement process to minimize their surface energies. As the prepared ZnO nanosheets, composed of ZnO nanoparticles, possess quite high surface energy due to the exposure of two main planes, thus the surface energies can be minimized by reducing the exposed areas through

the aggregation of the nanosheets. Consequently, by aggregating and self-assembling of the neighboring nanosheets, the surface energies of the system were significantly decreased. Therefore, the prepared porous ZnO nanosheets were self-assembling in a special way that rosette-like morphologies are formed. Further, as the growth velocities of ZnO crystals in various directions are different under hydrothermal condition, thus, the growth of ZnO crystals at different surfaces are not the same, hence nanosheets are formed in irregular sizes.[36(b)] This might be the reason that the nanosheets are possessing various sizes and therefore, the sizes of the final rosette-like morphologies are different which is evident from the observed FESEM results (fig. 1(a) and (b)).

For explaining the role of PEG, the hydrophobic head groups of PEG first facilitates the formation of aggregations in solution due to the incomplete mixing at the molecular level and the retention of remnants of the 3D hydrogen bonded network structure of bulk solution. These PEG aggregates acted as templates which lead to the formation of nanoparticles. These nanoparticles f urther undergo a multiplying growth through a cementing mechanism or oriental attachment and finally formed the sheet-like morphologies over the ITO substrate surface. It is reported that usually the pore diameter of the nanomaterials are associated to the size of hydrophobic aggregations.[36(a)] Further, the sizes of hydrophobic aggregations are depend on the molecular weight of PEG, i.e. with higher PEG molecular weight, larger hydrophobic aggregations can be produced. For the synthesis of porous ZnO nanosheets, high molecular weight (~100000) PEG was used which might create larger hydrophobic aggregates in the reaction solution and considerably forms the large pores and highly porous nanostructures. In addition, the hydrated zinc ions could be trapped in the hydrophobic PEG aggregates and mounted into large hydrophobic aggregations which might split into several smaller ones, and results in the

production of the small and highly dense pores in the final ZnO products.

To examine the influence of the reaction time on the growth of porous nanostructures, different hydrothermal experiments have been performed by varying the growth reaction times, i.e. 2, 4, 6, 8, 12, and 16 hrs at 150 °C. Figure 4 depicts the FESEM images of grown ZnO thin films with different reaction times. It is notable that the variation in reaction time has shown great impact on the porous nature of the final ZnO nanostructure. As evident from the Figure 4(a), the formation of ZnO nanosheets was started at a time of 2 h, indicating the emergence of nucleation sites. The nucleation of nanosheets continues with the increase of reaction time and highly porous, uniform and well-defined ZnO nanosheets are formed on the ITO substrate in 8 h, as shown in Figure 4(d). When the reaction time was further increases to 12 h (Fig. 4(e)), slight distortions in the porous nanosheet structures were observed. However, the basic nanosheet morphology was similar to the ones prepared at 8 hr reaction time. Further increasing the reaction time to 16 hrs, the nanosheets were almost completely deformed and it is very clear from the observed FESEM image (Fig. 4(e)) that the nanosheets are made of small nanoparticles. The reason for this drastic change might be related to the less entrapping of hydrated zinc ions with PEG molecules, which might result in the less formation of big hydrophobic PEG aggregations during the long reaction time. Therefore, the continuous and steady growth of porous ZnO nanostructures leads until the reaction time of 8 h and afterward, the system would be in closure-precipitation equilibrium stage, as depicted in Fig. 4(f).
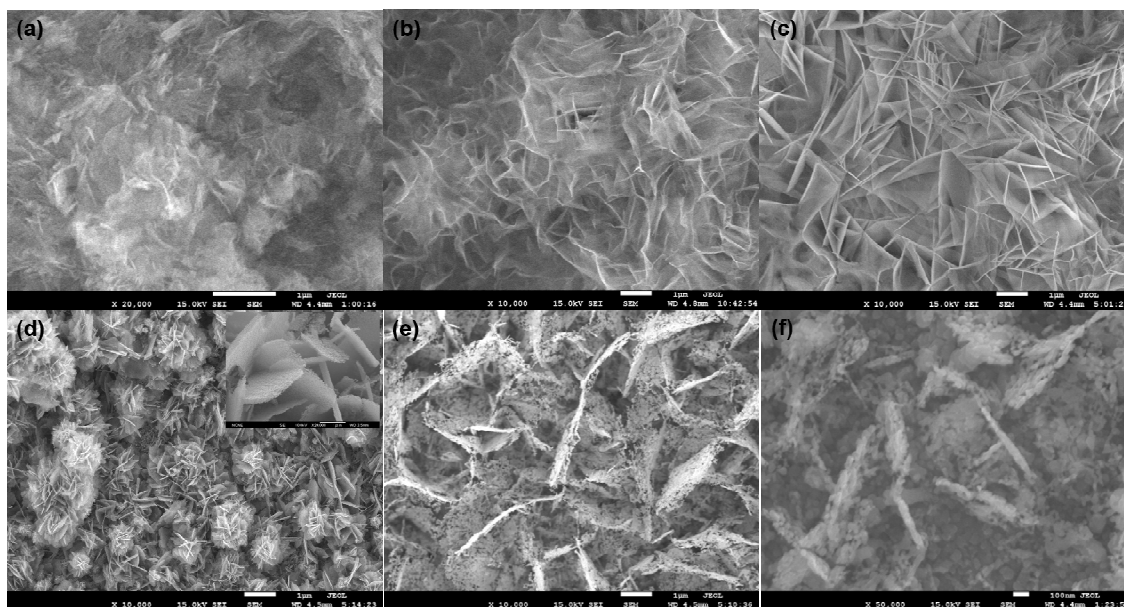
Figure 4: FESEM images of grown ZnO thin films with the reaction times of (a) 2h, (b) 4 h, (c) 6 h, (d) 8 h, (e) 12 h and (f) 16 h at 150°C.

Further, the elemental compositions of the grown highly porous ZnO nanosheets assembled in rosette like morphologies were characterized by energy dispersive spectroscopy (EDS) and the observed result is shown in figure 5 (a). For the EDS analysis, the deposited ZnO materials were detached from the ITO substrate and placed to the carbon tape and examined. The observed EDS spectrum revealed well-defined peaks for only zinc (Zn) and oxygen (O) which confirmed that the prepared nanosheets are mainly composed of Zn and O. No peak related with any impurity was seen in the observed spectrum which further confirmed the purity of prepared nanosheets.

To examine the crystallinity, crystal phases and structural properties, the deposited highly porous ZnO nanosheets assembled in rosette-like morphologies were further examined by X-ray diffraction (XRD). Figure 5 (b) exhibits the typical XRD pattern of prepared nanosheets which shows various well-defined diffraction reflections at $2\theta = 31.7^0$, 34.3^0, 36.2^0, 47.5^0, 56.5^0 and

63.1^0, corresponding to the wurtzite hexagonal phase of ZnO and can be assigned as ZnO(100), (002), (101), (102), (110) and (103), respectively. The observed diffraction reflections are well-matched with the reported Joint Committee on Powder Diffraction Standards (JCPDS) card no. 036-1451. In addition to the well-defined peaks related with ZnO, some other diffraction reflections related to the ITO substrate were also seen at 26.1^o, 33.7^o, 52.2^o and 62.7^o. Interestingly, all the observed diffraction reflections are sharp with high intensity, thus confirmed that the prepared porous nanosheets are well-crystalline.
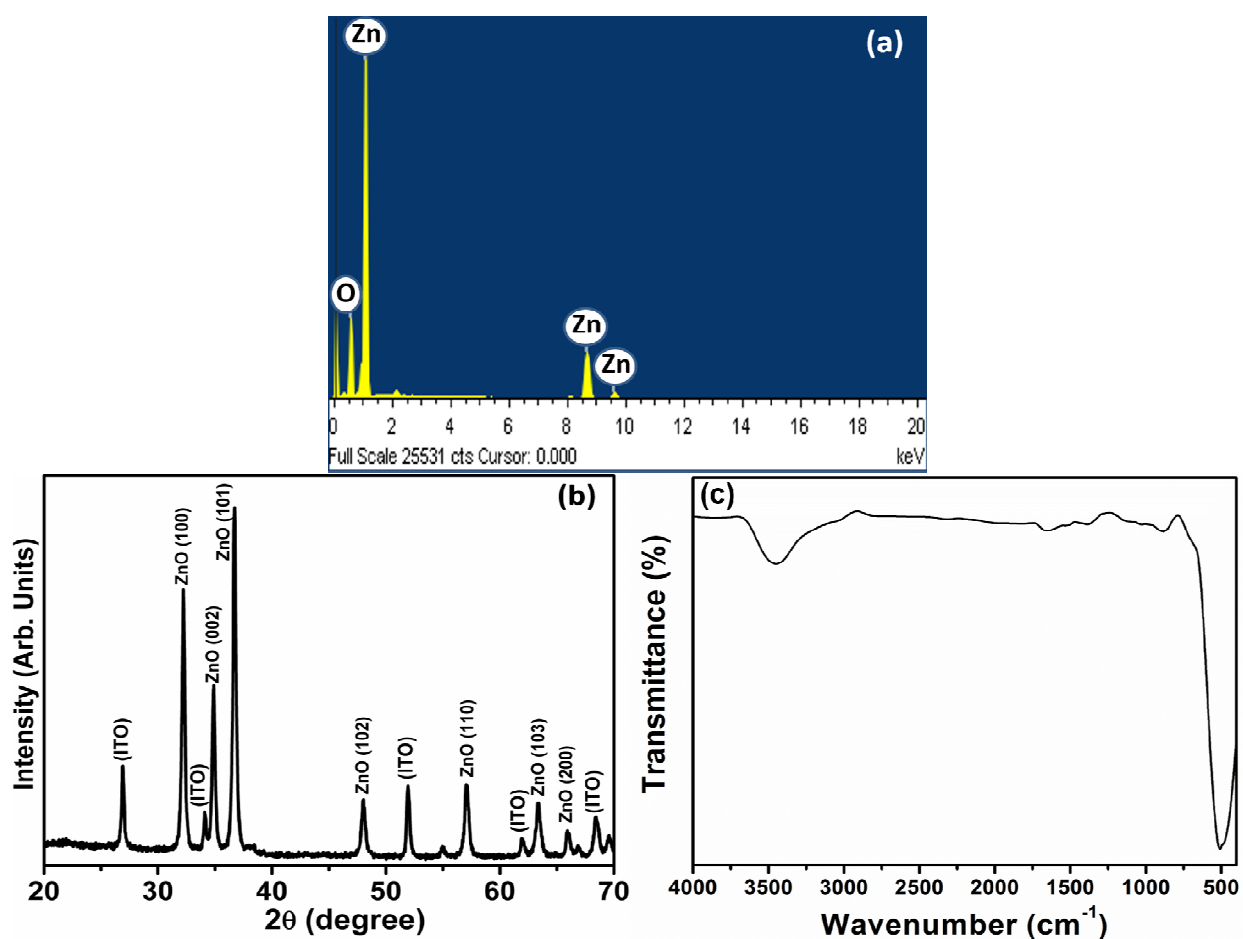

Figure 5: Typical (a) EDS spectrum, (b) XRD pattern and (c) FTIR spectrum of highly porous ZnO nanosheets assembled in rosette-like morphologies thin film grown on ITO substrate by hydrothermal process

-17-

Figure 5(c) shows the FTIR spectrum of grown highly porous ZnO thin film to define the structural and quality of the materials. The observation of an intense IR band at 483 cm^{-1} corresponds to the typical metal–oxygen (i.e. Zn–O), deducing the formation of ZnO.[37a] Two weak IR bands at 1641 and 1379 cm^{-1} are related to the fundamental O–H from the physiosorbed water over the surface and C-H str. Bond, respectively. A broad and small IR band at 3454 cm^{-1} is originated from the O–H stretching vibrations for porous ZnO materials.[37b] This observation clearly confirms the high purity of grown porous ZnO nanomaterials with few traces of carbon impurities.

To evaluate the structural and vibrational properties, the prepared porous ZnO nanosheets assembled in rosette like morphologies thin film was further characterized by Raman-scattering spectroscopy at room-temperature. Generally, the wurtzite hexagonal phase ZnO possess C_{6V}^4 (P6$_3$mc) space group having two formula units per primitive cells, in which all the atoms engrossed the C_{3V} symmetry. According to the group theory, eight set of optical phonon modes at Γ point of the Brillouin zone i.e. $\Gamma = A_1 + 2B_1 + E_1 + 2E_2$ are present in the ZnO in which A_1, E_1, and E_2 modes are Raman active while B_1 modes are silent.[37c] Figure S-2† exhibits the typical Raman-scattering spectrum of prepared highly porous ZnO nanosheets assembled in rosette-like morphologies. The observed Raman-scattering spectrum demonstrate several Raman shift peaks at 332, 437, 584 and 673 cm^{-1}. The existence of a sharp and strong peak at 437.4 cm^{-1} indicates the presence of high E_2 mode which assigned to ZnO non-polar optical phonon.[38] The appearance of sharp E_2 mode in the Raman spectrum is usually representative of the wurtzite hexagonal nature of ZnO materials. Further, a Raman peak appearing at 332 cm^{-1} in ZnO nanomaterials can be assigned as $E_{2H}–E_{2L}$ and it is believed that the origination of this peak confirmed the single and well-crystalline nature of prepared.[38] Two other small Raman peaks at

584 and 673 cm^{-1} can be assigned to the E_{1L} and A_1 phonon modes. This is believed that these peaks are usually corresponding to the structural disorder and impurities in grown ZnO materials.[38] Finally, the presence of strong and sharp Raman-active E_2 high mode and suppressed E_{1L} mode affirmed that the prepared nanosheets are well-crystalline and possessing wurtzite hexagonal phase structure.

The detailed chemical composition and state of elements of grown porous ZnO nanosheets assembled in rosette like morphologies thin film were elucidated by XPS spectroscopy. Figure 7(a) depicts the Zn 2p spectrum which exhibits the doublet binding energy peaks at ~1021.7 eV and ~1046.1 eV. The former and later binding energies are assigned to Zn $2p_{3/2}$ and Zn $2p_{1/2}$, with the binding energy difference of 24.4 eV which is very close to standard reference value for bulk ZnO.[39] The appearance of these binding energies in the Zn 2p spectrum are designated to the lattice zinc phases in ZnO.[40, 41]
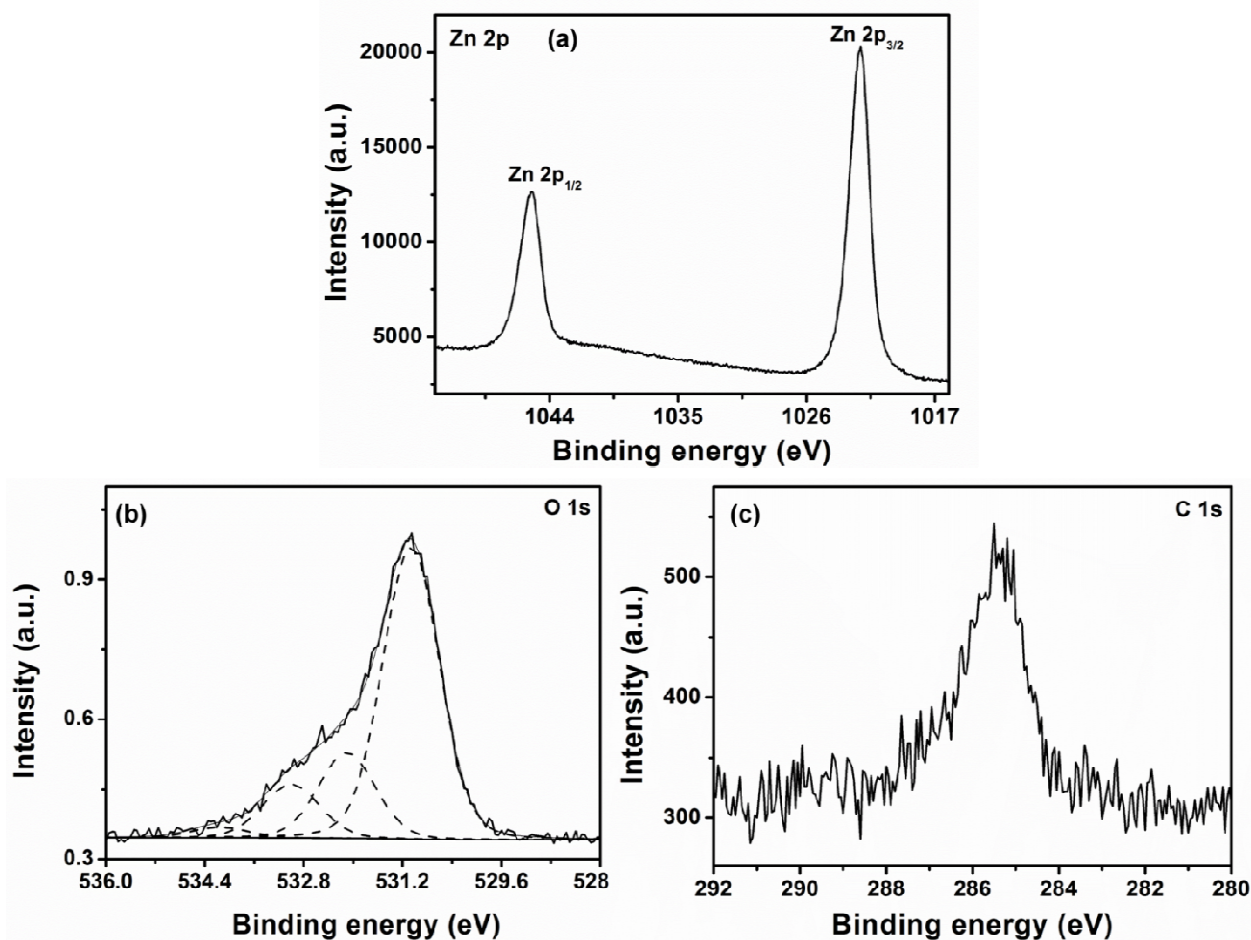
Figure 7: Typical XPS spectra of highly porous ZnO nanosheets assembled in rosette-like morphologies thin film grown on ITO substrate by hydrothermal process; (a) Zn 2p, (b) deconvulated O 1s, and (c) C 1s spectra.

Furthermore, the binding energy at ~1021.7 eV corresponds to the Zn^{2+} for typical wurtzite hexagonal structure of ZnO.[42] Thus, the obtained Zn 2p binding energy and the binding energy difference values deduce the +2 oxidation state Zn atoms in ZnO. The deconvolution of O 1s spectrum is shown in Fig. 7(b) which are composed of a center peak at ~531 eV with three deconvoluted binding energy peaks at ~532.1 eV, ~532.8 eV and ~533.9 eV. The main centered binding energy at ~531 eV corresponds to the existence of O^{2-} ions on the wurtzite structure of

the hexagonal Zn^{2+} ions and each O^{2-} ions are associated with nearest neighboring Zn atoms.[43] Other three binding energies at ~532.1 eV, ~532.8 eV and ~533.9 eV are imputed to the adsorbed moisture and few oxygen deficiency or oxygen vacancies within the ZnO materials. From Fig. 7(c), a broad binding energy at ~285.2 eV belongs to the C 1s is generally originated from the calibration analysis for other binding energies to avoid the specimen charging.[39] Thus, the strong Zn 2p and O 1s binding energies confirm the formation of pure ZnO materials by the association of Zn^{2+} and O^{2-} ions to form Zn–O bonds in ZnO crystals.

3.2. Dye-sensitized solar cell based on highly porous ZnO nanosheets thin film on ITO substrate

The prepared highly porous ZnO nanosheets assembled in rosette-like morphologies thin film grown on ITO substrate were directly used as photoanode to fabricate efficient DSSC. Figure 8(a) shows the typically current density–voltage (*J-V*) characteristics of the fabricated DSSC based on porous ZnO nanosheets photoanode. Several photovoltaic properties such as conversion efficiency (η), short-circuit current (J_{SC}), open-circuit voltage (V_{OC}) and fill factor (*FF*) of the fabricated DSSC can be calculated from the observed *J-V* curve. The calculated short circuit current (J_{SC}) and open circuit voltage (V_{OC}) for the fabricated DSSC, according to the observed J-V curve, are ~9.45 mA/cm^2 and 0.645 V, respectively. Further, the fill factor of the fabricated DSSC was calculated according to the equation (1) mentioned below:

$$FF = \frac{J_{max}V_{max}}{J_{SC}V_{OC}} \quad ....(1)$$

Here, J_{max} and V_{max} are the voltage and current density at maximum power output, respectively.

The calculated FF for the fabricated DSSC was found to be 0.55. Further, the light-to-

electricity conversion efficiency (η) of the fabricated DSSC based on highly porous ZnO nanosheets assembled in rosette-like morphologies thin film was also calculated using equation (2).

$$\eta = \frac{J_{SC} V_{OC} FF}{P_{in}} \quad ....(2)$$

Here, P_{in} is the power density of incident radiation.

Thus, the calculated light-to-electricity conversion efficiency for the fabricated DSSC was ~3.4%. The observed high light-to-electricity conversion efficiency of the fabricated DSSC based on highly porous ZnO nanosheets assembled in rosette like morphologies thin film was due to special morphology of the photoanode material. Such photoanode material with high porous nature and surface area significantly improves the performance and J_{SC} of the fabricated DSSC. Moreover, it is known that the high generation of photocurrent is usually associated with the film morphology, surface texturing, surface area and crystallinity of the photoanode materials.[44,45] From the surface analysis, it was observed that the grown highly porous ZnO nanosheets assembled in rosette like morphologies thin film exhibited reasonable surface area, i.e. ~26.7 m^2/g which provide a suitable environment for large amount of dye absorption (4.1 x 10^{-5} mol/cm^2) through their highly porous surfaces. Herein, the high surface area of ZnO thin film is proficient for the higher dye absorption and enhances the light harvesting efficiency of the photoanode.[46]

Table 1. Performance of the fabricated DSSC based on highly porous ZnO nanosheets assembled in rosette-like morphologies and other reported DSSCs fabricated using various ZnO nanostructures.

ZnO Morphology	Photovoltaic performances				Ref.
	J_{SC} (mA /cm^2)	V_{OC} (V)	FF	η (%)	
Nanoparticles	3.64	0.68	0.49	0.92	[7a]
Branched Nanowires	1.84	0.62	0.4	0.46	[20]
Nanoparticles	0.3704	0.4796	0.56	0.1	[21]
Nanorods	2.01-2.21	0.63-0.64	0.58-0.63	0.73-0.83	[22]
Nanorods	1.11-1.41	0.351- 0.387	0.461- 0.441	0.18-0.24	[24]
Nanorods	1.84	0.76	0.472	0.7	[52]
Nanorods	4.2	0.266	0.3	0.67	[53]
Nanofibres	2.87	0.69	0.44	0.88	[54]
Nanosheets	0.301	0.37	0.58	0.124	[55]
Nanocrystal	5.06	0.61	0.65	2.04	[56]
Microspheres	6.65	0.676	0.65	2.94	[57]
Nanorods	7.29	0.572	0.588	2.42	[58]
Highly porous nanosheets	**9.45**	**0.654**	**0.55**	**3.4**	**Present work**

Interestingly, from the literature, it was observed that the fabricated DSSC based on highly porous ZnO nanosheets assembled in rosette-like morphologies thin films is exhibiting superior photovoltaic properties compared to other ZnO based DSSCs reported in the literature[47-50], as compared in table 1.[7a, 20-22, 24, 52-58] Thus, it can be confirmed that the special morphology of the photoanode material, i.e. highly porous nanosheets structure, is one of the major factor for

enhanced J_{SC} and η of the fabricated DSSC.

Recently, Ganesh et al. have demonstrated that the choice of dye is one of the important parameters which severely effects the photovoltaic properties of fabricated DSSCs.[59] The authors showed that the power-conversion efficiencies of the fabricated DSSCs can be improved by applying appropriate dyes. Thus, using newly synthesized di-substituted tri-phenyl amine (HMP-9) and carbazole (HMP-11) dyes (with limited acidic carboxyl anchor groups), ZnO nanocrystallites based DSSC was fabricated which exhibited a power conversion efficiency of 7.03%.
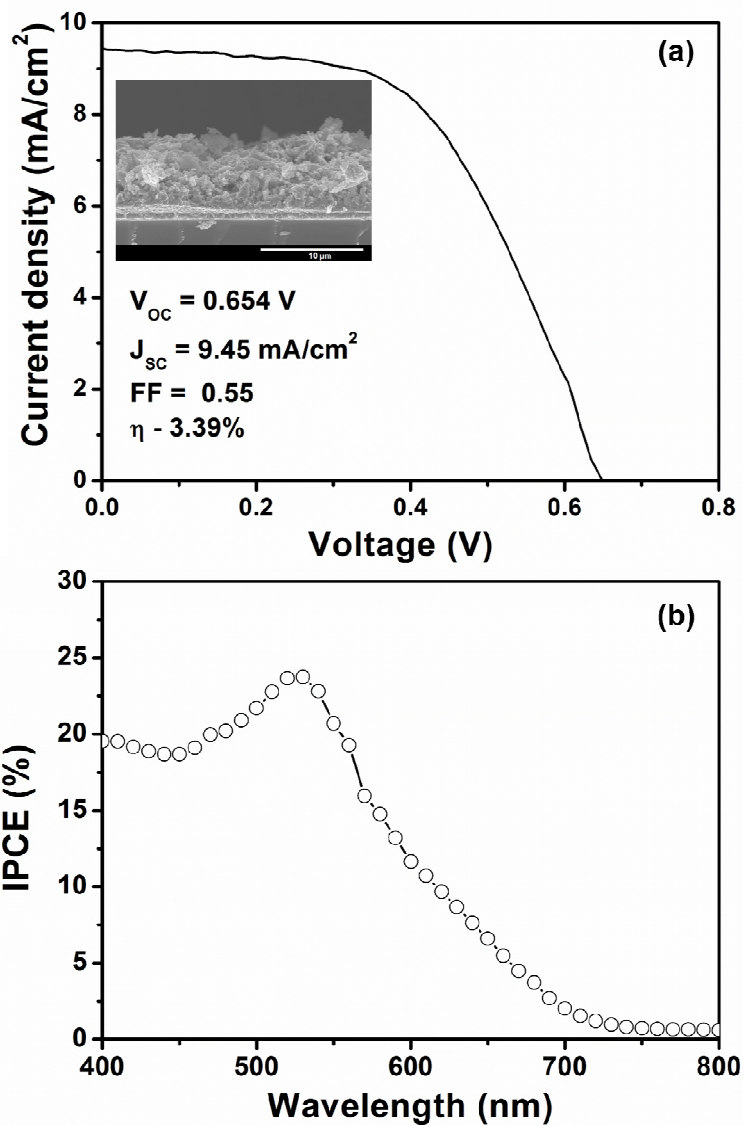
Figure 8: **(a)** Typical current-voltage (*J-V*) characteristics and **(b)** incident photon-to-current conversion efficiency (IPCE) characteristics of fabricated DSSC based on highly porous ZnO nanosheets assembled in rosette-like morphologies thin film based photoanode. Inset shows the cross-sectional image of the thin film.

The incident photon-to-current conversion efficiency (IPCE) was measured to find out the explanation of the high photocurrent density for fabricated DSSC based on highly porous

ZnO nanosheets assembled in rosette like morphologies thin film photoanode. The ratio between the number of generated charge carriers contributing to the photocurrent and the number of incident photons can be observed by IPCE which can be calculated at a particular wavelength using equation (3).

$$IPCE(\%) = \frac{1240(eV.nm) \times J_{SC}(\frac{\mu A}{cm^2})}{\lambda(nm) \times \phi(\frac{mW}{cm^2})} \times 100 ....(3)$$

Here, λ and P_{in} are the wavelength and the intensity of the monochromatic light, respectively while the J_{SC} is the short-circuit photocurrent density for mono-chromatic incident light. Figure 8 (b) exhibits the typical IPCE graph for the fabricated DSSC which revealed a broad absorption in the range of 450-650 nm with the reasonable maximum IPCE value of 24.8% at 520 nm. The observed moderate IPCE is attributed to the high dye absorption via the highly porous ZnO nanosheets assembled in rosette like morphologies thin film. It has been reported that ZnO materials at nanoscale size usually provide the larger surface area as well as the pathway for electron transport, resulting in the high J_{SC}.[51] Thus, the unique morphology, i.e. highly porous nanosheet structure, and high surface area of the photoanode might enhance the electron injection and charge-transfer efficiency which significantly improve the J_{SC} and η of the fabricated DSSC.

4. Conclusion

In summary, highly porous ZnO nanosheets assembled in rosette-like morphologies thin film was directly grown on transparent conducting glass substrate (ITO) using facile low-temperature hydrothermal process and used as photoanode for the fabrication of high efficient

DSSC. The grown highly porous nanosheets were examined in detail using several characterization techniques which revealed that the grown nanosheets are made by the accumulation of thousands of nanoparticles and possess good crystal quality. Further, because of the excellent morphological properties, i.e. highly porous and surface area, the fabricated DSSC exhibited a reasonable light-to-electricity conversion efficiency of ~3.4% with high J_{SC} of 9.45 mA/cm^2, V_{OC} of 0.654 and FF of 0.55. The presented results demonstrate that ZnO nanomaterials can efficiently be used as effective photoanode material to fabricate high efficient DSSCs.

Acknowledgements

References

1. (a) B. O'Regan and M.Grätzel, *Nature* 1991, **353,** 737–740; (b) X. Shi, X. Lu, Yang Shao, Shuxian Wei, Qing Zhu, Dongliang Jin, Zhigang Deng, and Wenyue Guo *Sci. Adv. Mater* 2014, **6**, 2595-2602; (c) H. Song, Huisu Jeong, Soong Ho Um, Heon Lee, and Gun Young Jung, *Sci. Adv. Mater.* 2014, **6**, 2517-2521; (d) S. Pradhan, S. Kumar, and A. Dhar, Sci. Adv. Mater. 2014, **6,** 1702-1707

2.(a) M. Grätzel, *Nature* 2001, **414**, 338–344; (b) T. H. Chiang, Chun Yu Liu, and Chun Hsiung Chen, *Sci. Adv. Mater.* 2014, **6,** 890-898 ; (c) G. Cheng, M. Shaheer Akhtar, O-Bong Yang, and Florian J. Stadler, *Sci. Adv. Mater.* 2014, **6,** 459-464; (d) Javier Navas, Teresa Aguilar, Concha

Fernández-Lorenzo, Rodrigo Alcántara, Desiré M. de los Santos, Antonio Sánchez-Coronilla, David Zorrilla, Jesús Sánchez-Márquez, and Joaquín Martín-Calleja, *Sci. Adv. Mater*. 2014, **6,** 473-482

3. A.Yella, H.W. Lee, H.N. Tsao, C.Y. Yi, A.K. Chandiran, M.K. Nazeeruddin, E.W. G. Diau, C.Y. Yeh, S.M. Zakeeruddin and M. Grätzel, Science 2011, **334**, 629–634

4. B.E. Hardin, H.J. Snaith and M.D. McGehee, Nat. Photonics 2012, **6**, 162–169

5. K. Naomi, S. Yuta, O. Hideo, O. Masataka and I. Shinzaburo, *Sol. Energy Mater. Sol. Cells* 2007, **91**, 1243.

6. S. Haiyan, W. Jonas, H. H. Christian and S.-M. Lukas. *Sol. Energy Mater. Sol. Cells* 2011, **95**, 3450.

7. a) K. Takayuki, K. Yoshitaka, Y. Takahiro and T. Kohshin. ACS Appl. Mater. Interfaces 2009, **1**, 2107. b) I.Y.Y. Bu, and M.T. Cole, Mater. Lett. 2013, **90**, 56.

8. X.J. Feng, K. Shankar, O.K.Varghese, M.Paulose, T.J. Latempa and C.A.Grimes, *Nano Lett.* 2008, **8**, 3781–3786.

9. A.Z. Hu, L.X. Xiao, G.P. Dai and Z.C. Xia, *J. Solid State Chem.* 2012, **190**, 130–134.

10. (a) I. Chung, B. Lee, J. He, R.P.H. Chang and M.G. Kanatzidis, *Nature*, 2012, **485**, 486–489. (b) A R. Rao and V. Dutta, *Nanotechnology*, 2008, **19**, 445712

11. Ed. Ahmad Umar, Y. B. Hahn, "Metal oxide nanostructures and their applications", American Scientific Publishers (2010), Los Angeles, USA.

12. (a) A. Anta, E. Guillén, and R.T. Zaera, *J. Phys. Chem. C*, 2012, **116**, 11413-11425, F. Xu and L.Sun, *Energy Environ. Sci.* 2011, **4**, 818-841. (b) G.-C. Yi, C. Wang, and W. I. Park, *Semicond. Sci. Technol.* 2005, **20**, S22–S23

13. T. Minami, *J. Vac. Sci. Technol. A* 1999, **17**, 1765.

14. S. Ameen, M. S. Akhtar, M. Nazim and H.-S. Shin, *Mater. Lett.* 2013, **96**, 228–232

15. S. H. Kim, A. Umar, M. S. Akhtar, G. N. Dar and S. W. Hwang, *Sci. Adv. Mater.* 2014, **6**, 562-568.

16. K. S.Weissenrieder and J. Muller, *Thin Solid Films* 1997, **300**, 30.

17. C. M. Mo, Y. H. Li, Y. S. Lin, Y. Zhang and L. D. Zhang, *J. Appl. Phys.* 1998, **83**, 4389

18. a) M. Grätzel, *Prog. Photovolt. Res. Appl.* 2000, **8**, 171. b) P. P. Das, S. A. Agarkar, S. Mukhopadhyay, U. Manju, S. B. Ogale and P. S. Devi, *Inorg. Chem.*, 2014, **53 (8)**, 3961–3972.

19. a) Y. F. Hsu, Y. Y. Xi, A. Djurisic and W. K. Chen, *Appl. Phys. Lett.* 2008, **92**, 133507. b) A. Jana, P. P. Das, S. A. Agarkar, and P. S. Devi, *Solar Energy*, 2014, **102**, 143-151.

20. D. I. Suh, S. Y. Lee, T. H. Kim, J. M. Chun, E. K. Suh, O. B. Yang and S.-K. Lee, *Chem. Phys. Lett.* 2007, **442**, 348.

21. R. Parthiban, D. Balamurugan, and B.G. Jeyaprakash, *Spectrochim. Acta Part A: Mol. Biomol. Spectroscopy B* 2015, **136 (5)**, 986.

22. M. Raja, N. Muthukumarasamy, D. Velauthapillai, R. Balasundaraprabhu, S. Agilan, and T.S. Senthil, *Solar Energy* 2014, **106**,129.

23. A.J. Cheng, Y. Tzeng, Y. Zhou, M. Park, T. Wu, C. Shannon, D. Wang and W. Lee, *Appl. Phys. Lett.* 2008, **92**, 92113.

24. Y. Meng, Y. Lin, and Y. Lin, *Ceram. Inernational* 2014, **40 (1)**, 1693.

25. A. D. Pasquier, H. Chen and Y. Lu, *Appl. Phys. Lett.* 2006, **89**, 253513.

26. J.B. Baxter and E.S. Aydil, *Appl. Phys. Lett.* 2005, **86**, 53114.

27. a) M. Law, L.E. Greene, J.C. Johnson, R. Saykally and P.D. Yang, *Nat. Mater.* 2005, **4**, 455. b) R. Ramakrishnan , A. Aravind , S. J. Devaki, M. R. Varma, and K. Mohan, *J. Phys. Chem. C*, 2014, **118 (34)**, 19529-19539

28. A. Suliman, Y. Tang and L. Xu, *Sol. Energy Mater. Sol. Cells* 2007, **91**, 1658.

29. Ahmad Umar, A. Al-Hajry, Y. B. Hahn, D. H. Kim, *Electrochimica Acta*, 2009, **54**, 5358–5362.

30. C. Lin, H. Lin, J. Li and X. Li, *J. Alloys Compd.* 2008, **462**, 175

31. A. Umar, C. Ribeiro, A. Al-Hajry, Y. Masuda and Y. B. Hahn, *J. Phys. Chem. C* 2009, **113**, 14715–14720

32. T. R. Giraldi, G.V. F. Santos, V.R. Mendonça, C. Ribeiro and I.T. Weber, *J. Nanosci. Nanotech.,* 2011, **11**, 3635–3640.

33. T. M. Milao, V. R. de Mendonça, V. D. Araújo, W. Avansi, C. Ribeiro, E. Longo and M. I. Bernardi, *Sci. Adv. Mater.* 2012, **4**, 54–60.

34. S. Liufu, H. Xiao and Y. Li, *Powder Tech.* 2004, **145**, 20– 24

35. Z. Li , Y. Xiong and Y. Xie, *Inorg. Chem.* 2003, **42**, 8105 − 8109)

36. a) Y. Jia, X.-Y. Yu, T. Luo, M.-Y. Zhang, J.-H. Liu and X.-J. Huang, *CrystEngComm*, 2013, **15**, 3647-3653), b) R. A. Laudise, A.A. Ballman. *J. Phys. Chem.* 1960, **64**, 688.

37. a) M. S. Chauhan, R. Kumar, A. Umar, S. Chauhan, G. Kumar, S. W. Hwang, A. Al-Hajry, *J. Nanosci. Nanotechnol.* 2011, **11**, 4061. b) N. Kannadasan, N. Shanmugam, S. Cholan, K. Sathishkumar, G. Viruthagiri, R. Poonguzhali, Mater. Charact. 2014, **97**, 37. c) J. M. Calleja and M. Cardona, *Phys. Rev. B* 1977, **16**, 3753.

38. A. Umar and Y.B. Hahn, *Nanotechnology* 2006, **17**, 2174.

39. C.D. Wagner, W.M. Riggs, L.E. Davis, J.F. Moulder and G.E. Muilenberg, Handbook of X-ray Photoelectron Spectroscopy, Perkin Elmer, Eden Prairie, 1979.

40. N.S. Ramgir, D.J. Late, A.B. Bhise, M.A. More, I.S. Mulla, D.S. Joag and K. Vijayamohanan, *J. Phys. Chem. B* 2006, **110**, 18236–18242.

41. C.Y. Leunga, A.B. Djurisic, Y.H. Leung, L. Ding, C.L. Yang and W.K. Ge, *J. Cryst. Growth* 2006, **290**, 131–136

42. W.J. Li, E.W. Shi, W.Z. Zhong, Z.W. Yin, *J. Cryst. Growth* 1999, **203**, 186–196

43. J.C.C. Fan, J.B. Goodenough, *J. Appl. Phys.* 1977, **48**, 3524–3531

44. T.V. Nguyen, H.C. Lee and O.B. Yang, *Sol. Energy Mater. Sol. Cells* 2006, **90**, 967.

45. E. Hosono, S. Fujihara and T. Kimura, *Electrochim. Acta* 2004, **49**, 2287

46. A.D. Pasquier, H. Chen and Y. Lu, *Appl. Phys. Lett.* 2006, **89**, 253513

47. Y. Meng, Y. Lin, Y. Lin and J. Yang, *J. Solid State Chem.* 2014, **210**, 160–165

48. Q. Hou, L. Zhu, H. Chen, H. Liu and W. Li, *Electrochimica Acta* 2013, **94**, 72–79

49. A. E. Suliman, Y. Tang and L. Xu, *Sol. Energy Mater. Sol Cells*, 2007, **91**, 1658-1662

50. Z. Liu, Y. Li, C. Liu, J. Ya, W. Zhao, L. E, D. Zhao and L. An, *Solid State Sciences*, 2011, **13** 1354-1359

51. Q. Zhang, C.S. Dandeneau, X. Zhou and G. Cao, *Adv. Mater.* 2009, **21**, 4087.

52. A. Al-Hajry , A. Umar, Y. B. Hahn, and D.H. Kim, *Superlattices and Microstruct.* 2009, **45**, 529.

53. L. Ke , S. B. Dolmanan, L. Shen, P. K. Pallathadk, and Z. Zhang, *Sol. Energy Mater. Sol. Cells,* 2010, 94, 323.

54. S. Li, X. Zhang, X. Jiao, and H. Lin, *Mater. Lett.* 2011, **65**, 2975.

55. S. Suresh, A. Pandikumar, S. Murugesan, R. Ramaraj, and S. P. Raj, *Solar Energy* 2011, **85**, 1787.

56. V. Devabharathi, K.L. Palanisamy, and N. M. Sundaram, *Superlattices and Microstructures* 2014, **75,** 99.

57. Y. Meng, Y. Lin, Y. Lin, and J. Yang, *Journal of Solid State Chemistry* 2014, **210**, 160.

58. Y. Meng, Y. Lin, and J. Yang, *Applied Surface Science* 2013, **268**, 561.

59. T. Ganesh, H.-M. Nguyen, R. S. Mane, N. Kim, D. V. Shinde, S. S. Bhande, M. Naushad, K.

N. Hui and S. H. Han, *Dalton Trans.*, 2014, **43**, 11305–11308.